Acta Materialia 212 (2021) 116916

Contents lists available at ScienceDirect

Acta Materialia

journal homepage: www.elsevier.com/locate/actamat

Full length article

Vapor phase dealloying kinetics of MnZn alloys

Zhen Lu[a,b], Fan Zhang[a], Daixiu Wei[c], Jiuhui Han[a], Yanjie Xia[a], Jing Jiang[c], Mingwang Zhong[d], Akihiko Hirata[a,b], Kentaro Watanabe[a], Alain Karma[d,*], Jonah Erlebacher[e,*], Mingwei Chen[a,e,*]

[a] Advanced Institute for Materials Research, Tohoku University, Sendai 980-8577, Japan
[b] Mathematics for Advanced Materials Open Innovation Laboratory, AIST, 2-1-1 Katahira, Aobaku, 980-8577 Sendai, Japan
[c] Institute for Materials Research, Tohoku University, Sendai, 980-8577, Japan
[d] Department of Physics and Center for Interdisciplinary Research on Complex Systems, Northeastern University, Boston, MA, USA
[e] Department of Materials Science and Engineering, the Johns Hopkins University, Baltimore, MD 21218, USA

ARTICLE INFO

Article history:
Received 23 October 2020
Revised 14 April 2021
Accepted 15 April 2021
Available online 22 April 2021

Keywords:
Vapor phase dealloying
Dealloying kinetics
Ballistic evaporation
Knudsen diffusion
Activation energy

ABSTRACT

Vapor phase dealloying (VPD) is an environmentally-friendly method for fabricating nanoporous materials by utilizing the saturated vapor pressure difference of elements to selectively drive sublimation of one or more components from an alloy. VPD kinetics has not been explored and rate-controlling factors of the solid-gas transformation within complex nanostructure remain unknown. Using manganese-zinc alloys as a prototype system, we systematically investigated the dependence of dealloying velocity on temperature and pressure and presented a model to quantitatively describe the dealloying kinetics. We found that the dealloying velocity exhibits a linear to power law transition at a critical dealloying depth, resulting from the interplay between the kinetic process of dealloying and dealloyed microstructure. This transition bridges ballistic evaporation at early time to Knudsen diffusion of Zn vapor in developed pore channels where the Zn partial pressure at the dealloying front reaches the local equilibrium between the solid and vapor phases. By comparing activation energies for VPD and bulk zinc sublimation, the entire energy landscape of VPD is measured. The fundamental understanding of VPD kinetics paves an effective way to design dealloyable precursor alloys and to optimize dealloyed microstructure of VPD materials for a wide range of applications.

1. Introduction

Dealloying is a convenient process to fabricate bicontinuous porous structures with a large specific surface area [1], a high density of low-coordinated surface atoms [2] and high electrical and thermal conductivities [3,4]. Dealloyed porous materials have been explored in a wide range of applications including catalysis [5–8], actuation [9], sensors [10], energy storage and conversion [11–14], *etc.* In traditional electrochemical dealloying (ECD), selective etching and nanopore formation are driven by the standard electrode potential difference between pore-forming metals and sacrificial components in precursor alloys [15–17]. Because of the requirement of electrochemical corrosion, the resulting nanoporous materials are mainly noble metals, such as Au, Pt, Pd, Cu, etc [1,4,18–20]. A second approach, liquid metal dealloying (LMD), has been developed as a facile method to fabricate porous materials from light metals to inorganic materials by using the difference in miscibility of alloy components in metallic baths [21–25]. However, high dealloying temperatures in LMD often lead to coarsened porosity and the technique requires a post-processing chemical corrosion to excavate the porous structure from solidified metal baths [21]. Very recently, vapor phase dealloying (VPD) has emerged as a versatile and environmentally-friendly method to fabricate porous materials [26,27]. VPD utilizes the saturated vapor pressure (SVP) difference between constituent elements in an alloy and selectively sublimates a high SVP element(s) at appropriate temperatures and vacuum conditions, accompanied by the spontaneous reorganization of the residual elements to form a porous structure with bicontinuous open porosity [26,27].

The formation of nanoporosity during dealloying is often described as the competition between selective dissolution of sacrificial elements from precursor alloys to surrounding media and the reorganization of the remaining components at the dealloying front to form the backbone of the porous structure [15,28–33]. In general, dealloying kinetics is possibly governed by two factors: diffusion (or re-organization) of pore forming elements at the interface

* Corresponding author.
E-mail addresses: alainkarma@gmail.com (A. Karma), jonah.erlebacher@jhu.edu (J. Erlebacher), mwchen@jhu.edu (M. Chen).

https://doi.org/10.1016/j.actamat.2021.116916
1359-6454/

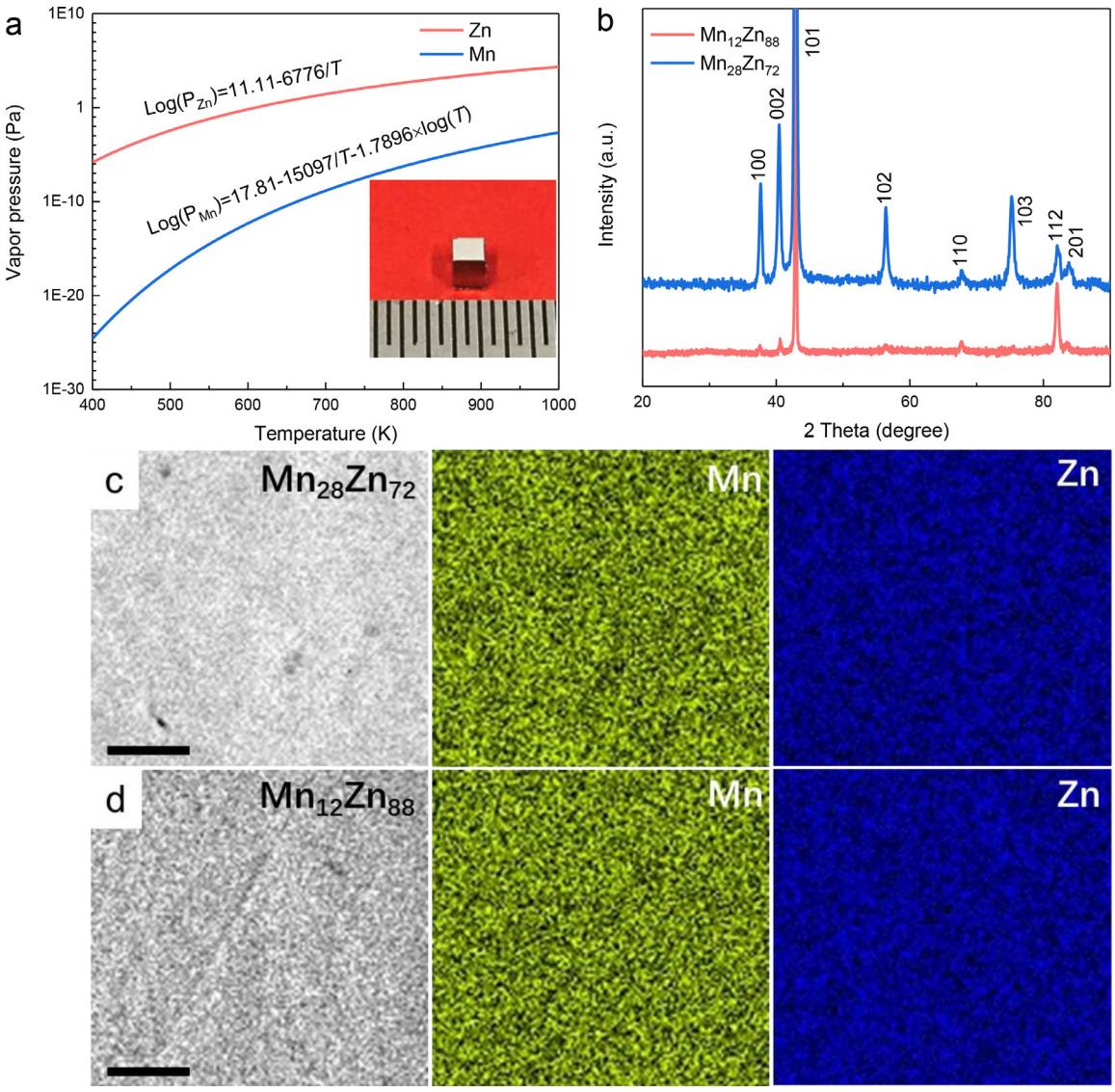

Fig. 1. (a) The relation between temperature and SVP of Zn and Mn. The inset shows the photo of a polished $Mn_{28}Zn_{72}$ precursor sample. (b) XRD patterns of $Mn_{28}Zn_{72}$ and $Mn_{12}Zn_{88}$ precursor samples exhibiting a single hexagonal close-packed phase. (c) and (d) The EDS mappings of $Mn_{28}Zn_{72}$ and $Mn_{12}Zn_{88}$ precursors with homogeneously elements distribution, respectively. Scale bar: 10 μm.

between precursor alloys and the dealloying media, and the transport of sacrificial elements from the precursor alloy to the dealloying media, both driven by high chemical potentials at dealloying fronts [15,21]. Sacrificial element transport can be controlled by the slowest step of diffusion during dealloying and the reactions at dealloying fronts, depending on the systems under investigation [21,30,32]. In ECD, the influence of the sacrificial element transport on dealloying kinetics is often minimal because of the facile oxidation and fast diffusion of sacrificial element ions in aqueous electrolytes. As a result, the interface velocity in ECD is usually controlled by the dissolution rate at the electrode/electrolyte interfaces and exhibits linear dealloying kinetics [34,35]. For LMD, it has been found that diffusive transport of the sacrificial elements away from the dealloying fronts is much slower than in ECD. LMD systems tend to exhibit long-range diffusion limitations with the dealloying interface velocity slowing down as a power law [21,22,36]. Although it has been found that nanopore formation during VPD can be regulated by the pressure of a dealloying chamber, dealloying temperature and dealloying time [26], the dealloying kinetics of VPD has not been systematically studied and a model that describes the dealloying process of VPD has not been developed. In contrast with ECD and LMD [37], the dealloying conditions, *i.e.*, temperature and pressure, of VPD can be tuned over a wide range, which provides a unique opportunity to explore the influence of mass transport on dealloying kinetics. Considering that porous Mn has not been successfully fabricated by ECD and VPD and, technically, multi-valence Mn and Mn compounds are important electrode materials for batteries and supercapacitors, in this study we chose $Mn_{28}Zn_{72}$ and $Mn_{12}Zn_{88}$ alloys as the model systems to investigate the VPD kinetics (dealloying velocity and porosity evolution) as they vary with composition, dealloying time, temperature and pressure.

2. Methods

Binary $Mn_{28}Zn_{72}$ and $Mn_{12}Zn_{88}$ (atomic ratio) alloys were prepared by induction heating from Mn (99.9+%, Nilaco Co.) and Zn (99.5%, Nilaco Co.) lumps under the protection of Argon with pos-

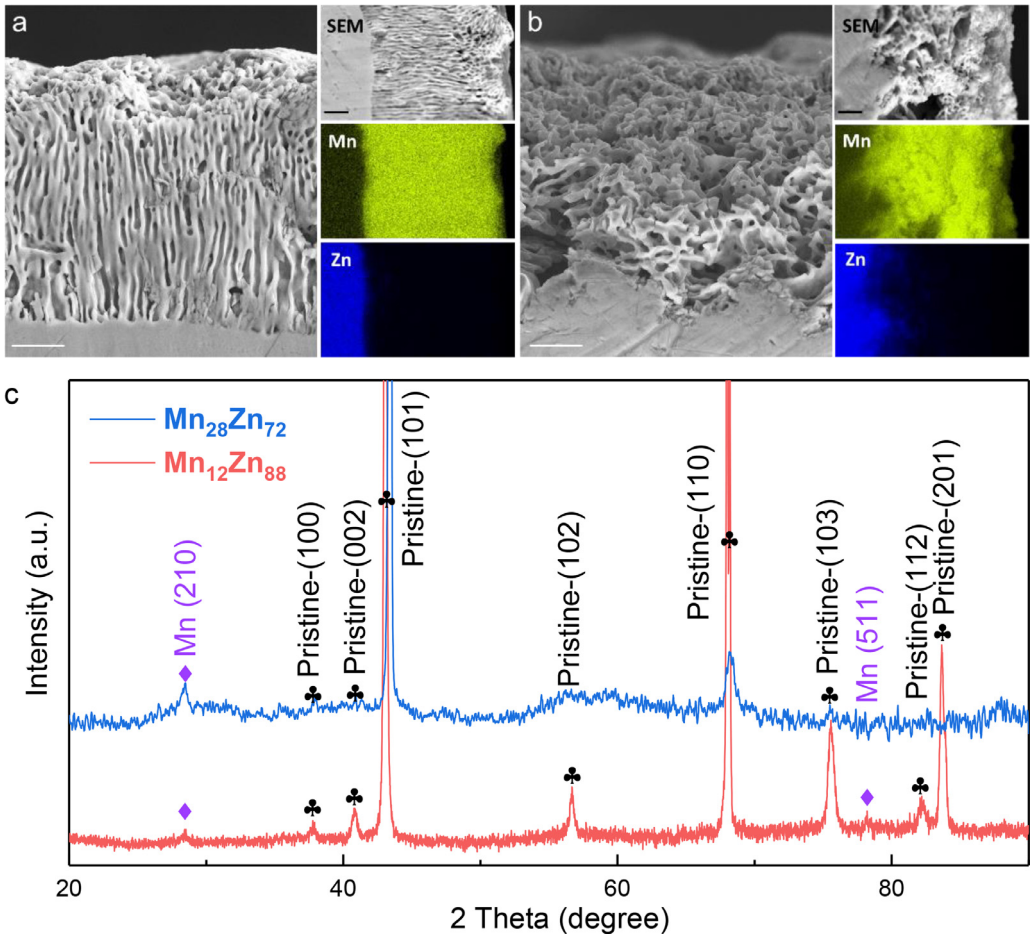

Fig. 2. (a) and (b) The SEM cross-sectional images and the corresponding EDS chemical mappings of partially dealloyed $Mn_{28}Zn_{72}$ and $Mn_{12}Zn_{88}$ samples at 673 K and 200 Pa for 180 min and 60 min, respectively. Scale bar: 5 μm. (c) XRD profiles of partially dealloyed $Mn_{28}Zn_{72}$ and $Mn_{12}Zn_{88}$ samples at 673 K for 30 min at 200 Pa.

itive pressures. On account of the large difference in the boiling points and saturated vapor pressures of Zn and Mn, the initially prepared compositions were $Mn_{23}Zn_{77}$ and Mn_9Zn_{91} (atomic ratio) with the total mass of 20 g per batch to produce the targeted compositions of $Mn_{28}Zn_{72}$ and $Mn_{12}Zn_{88}$, respectively. Cube-shaped samples with dimensions of 1.5 mm × 1.5 mm × 1.0 mm were cut by a diamond wheel saw and carefully polished with 0.05 μm Al_2O_3 powder to obtain mirror-finished surfaces. The precursor samples were dealloyed at a series of temperatures under low vacuum in a home-built vacuum dealloying system consisting of a high-temperature tube furnace, a condensation unit and a vacuum system with pressure adjustable from 1000 Pa to 2×10^{-4} Pa (Supplementary Fig. S1). To maintain a reducing atmosphere, the vacuum chamber was fed with flowing mixture gas of 200 sccm Ar and 10 sccm H_2. During the heating process, a constant temperature ramping of 20 K/min was used and the temperature fluctuation of the tube furnace was within 1 K for the isothermal heating process.

The crystal structures of $Mn_{28}Zn_{72}$ and $Mn_{12}Zn_{88}$ samples were characterized by X-ray diffraction (XRD) with Cu-K_α radiation (Rigaku SmartLab 3 kW). The microstructure and chemical composition of the samples were investigated using a field-emission scanning electron microscope (SEM, JEOL JIB-4600F, 15 keV) equipped with an X-ray energy-dispersive spectroscopy (EDS) system. One side of a dealloyed sample was carefully polished to show the dealloying depth, which was calculated from the measured dealloyed area divided by sample widths to achieve an unbiased value. Meanwhile, averaging ~30 measurements of dealloying depth from SEM images were recorded, and the calculated standard deviation was given as the error bars of plots. The diffusion-limited master curves were collapsed by re-scaled time $t' = t \times \exp(-E/k_BT)$ from a fundamental thermodynamic equilibrium property and the fitting values of activation energy E were derived by genetic algorithm.

3. Results

3.1. Microstructural evolution during dealloying

Fig. 1a shows the temperature dependence of the SVP of zinc and manganese [38]. The large SVP difference between zinc and manganese over a wide temperature window suggests that a series of convenient dealloying conditions can be employed to selectively remove Zn from the precursor alloys to form porous Mn. The dealloying kinetics of the two alloys were investigated at three temperatures of 653 K, 673 K and 723 K and two pressures of 200 Pa and 2×10^{-4} Pa. The dealloying experiments include three stages: heating at a constant ramping rate of 20 K/min to designated temperatures; maintaining temperature for different periods of time; and fast cooling. The cross-sections of dealloyed samples were characterized by SEM to measure dealloying depths and the morphology of resulting porous microstructures. Fig. 1b shows the XRD spectra of $Mn_{28}Zn_{72}$ and $Mn_{12}Zn_{88}$ samples after heating to 673 K at a dealloying pressure of 200 Pa and immediately cooled to room temperature. The heating and cooling cycle does not bring any structural changes of the two precursor alloys. Both $Mn_{28}Zn_{72}$

and $Mn_{12}Zn_{88}$ have a hexagonal close-packed (HCP) structure. EDS mappings show that Mn and Zn are homogeneously distributed in the alloys (Fig. 1c and d). Obvious pores cannot be found on the sample surfaces after the cycle of temperature rise and cooling at the pressures of 200 Pa (Supplementary Fig. S2).

Fig. 2a and b are the SEM cross-sectional images and EDS chemical mappings taken from $Mn_{28}Zn_{72}$ and $Mn_{12}Zn_{88}$ samples, dealloyed at 673 K and 200 Pa for 180 min and 60 min, respectively. The dealloyed porous region of $Mn_{28}Zn_{72}$ has a relatively sharp interface with the solid precursor alloy compared to that of $Mn_{12}Zn_{88}$. Correspondingly, significant chemical composition changes can be detected in the porous regions, which are enriched with Mn. The residual concentrations of zinc in the porous regions of the $Mn_{28}Zn_{72}$ and $Mn_{12}Zn_{88}$ samples are 1.9 at.% and 4.6 at.%, respectively. XRD spectra of partially dealloyed samples show the appearance of body-centered cubic (BCC) Mn peaks (Fig. 2c), further demonstrating the formation of porous Mn by VPD. From both SEM-EDS chemical mappings and XRD spectra, an intermediate phase cannot be seen and it suggests the direct transition from the precursor HCP Zn-Mn alloys to the porous BCC Mn by selectively evaporating Zn. Obviously, the two dealloyed samples present divergent porous morphologies. $Mn_{12}Zn_{88}$ has a spongy microstructure with a pore size around 500 - 700 nm while the dealloyed $Mn_{28}Zn_{72}$ sample shows anisotropic porosity, with a long narrow channel structure and a pore diameter of about 300 - 500 nm (Fig. 2a and b). Therefore, the precursor compositions apparently influence the dealloyed microstructures.

3.2. The dependence of dealloying depth on time, temperature and pressure

Dealloying kinetics was investigated by measuring the time dependence of dealloying depth at different pressures and temperatures. From the polished surfaces of partially dealloyed samples, the dealloying depth can be visualized and measured as shown in the inset of Fig. 3a. At a constant dealloying pressure of 200 Pa, the dealloying depth increases with time and temperature (Fig. 3a). Log-log plots of this data are straight lines, showing a power law relationship between dealloying depth and time. The nearly constant slopes of ~0.4 for both $Mn_{28}Zn_{72}$ and $Mn_{12}Zn_{88}$ alloys are independent of dealloying temperatures (Fig. 3b). The power-law relation indicates that the dealloying front migration is more likely dominated by a long-range diffusion process, rather than interface diffusion and reaction [21,36]. In spite of the identical power-law exponent of the two alloys at 200 Pa, the dealloying rates, defined by the dealloying depth per second, strongly depend on the dealloying temperatures and the compositions of precursor alloys (Fig. 3a and b). High dealloying temperatures promote faster porous layer growth. Moreover, the $Mn_{12}Zn_{88}$ alloy with more Zn has an obviously higher dealloying rate than $Mn_{28}Zn_{72}$ under the same dealloying temperatures, which is in line with the relatively large pore size of dealloyed $Mn_{12}Zn_{88}$.

Fig. 4a shows the relation between dealloying time and depth of $Mn_{28}Zn_{72}$ at 673 K under two different pressures of 200 Pa and 2×10^{-4} Pa. The higher-vacuum condition exhibits a relatively higher dealloying rate across the entire dealloying period. In comparison with the low-vacuum power-law time-depth curve, the high-vacuum dealloying time-depth plot shows an apparent linear period up to the dealloying depth of ~29.5 μm at the dealloying time of ~7,200 seconds. Because the linear period is much longer than the temperature ramping time of 1,200 seconds before dealloying, it cannot be attributed to any pore pre-formation reaction during sample heating. The existence of the linear period can also be identified from the log-log plot of dealloying time-depth curves (Fig. 4b), which presents a distinct discontinuity in the dealloying kinetics in the early stage of dealloying under the low dealloying

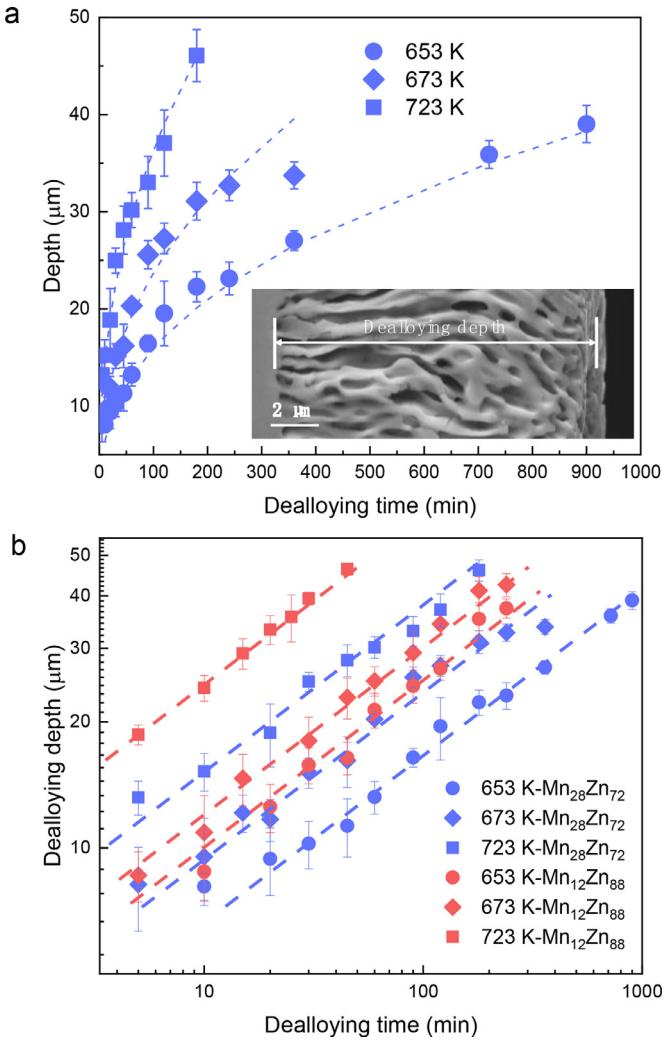

Fig. 3. (a) The relation between dealloying depth and time at 200 Pa and different temperatures for $Mn_{28}Zn_{72}$. The inset shows the measurements of dealloying depth from the cross-section of partially dealloyed $Mn_{28}Zn_{72}$ samples. (b) Correlation between dealloying time and depth at 200 Pa and different temperatures. The dashed lines show the same exponent value of 0.4 for both $Mn_{12}Zn_{88}$ and $Mn_{28}Zn_{72}$.

pressure. After ~7,200 seconds the dealloying time-depth curves of both 200 Pa and 2×10^{-4} Pa can be well fitted by a power law relation with the exponent of ~0.4 (Fig. 4b). It appears that there is a transition of dealloying kinetics from linear to power-law relations with increasing dealloying depth under a low pressure of 2×10^{-4} Pa in the initial stage of dealloying.

This depth-dependent dealloying kinetics is further demonstrated by the time-depth curves at different dealloying temperatures in both $Mn_{28}Zn_{72}$ and $Mn_{12}Zn_{88}$ alloys under the low pressure of 2×10^{-4} Pa (Fig. 4c). Although the linear portions are difficult to distinguish from the initial stage of the power law relation in some plots, the noticeable deviation from the power law in the log-log plots as well as the different tendency from the 200 Pa data plots (Fig. 4b) indicates the initial stage of dealloying at the low pressure of 2×10^{-4} Pa does not follow the power law relation with the exponent of ~0.4. We noticed that the linear dealloying process is more obvious at lower dealloying temperatures for both $Mn_{28}Zn_{72}$ and $Mn_{12}Zn_{88}$ alloys as the slower dealloying rates give longer linear dealloying time in the dealloying depth-time plots. We have enlarged the linear portion to show the transition from linear to power law relation in Fig. 4d. The critical depths for the transition were carefully measured with the esti-

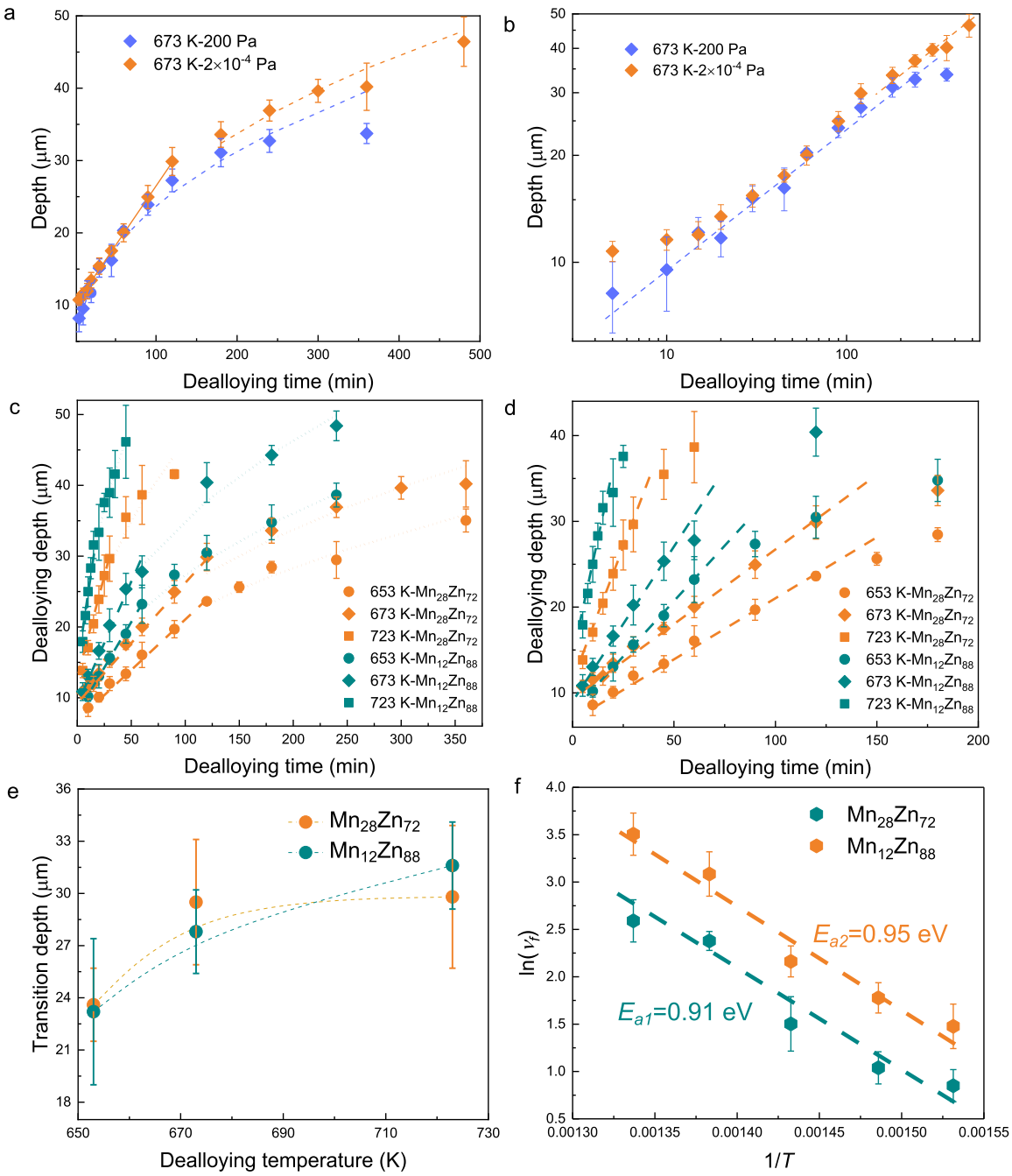

Fig. 4. (a) The relationship between dealloying depth and time at 673 K with different environmental pressures of $Mn_{28}Zn_{72}$. The yellow and blue dotted curves with the same exponent value of 0.4 and the yellow solid line is a guide to the eye. (b) A converted log-log plot of Fig. 4a. (c) Evolution of dealloying depth with a series of dealloying periods and temperatures at 2 × 10^{-4} Pa for $Mn_{12}Zn_{88}$ and $Mn_{28}Zn_{72}$. The green and yellow dashed lines and dotted curves are a guide to the eye. (d) The enlargement of the linear parts from Fig. 4 c for $Mn_{12}Zn_{88}$ and $Mn_{28}Zn_{72}$. (e) The correlation of transition depth with dealloying temperatures for $Mn_{12}Zn_{88}$ and $Mn_{28}Zn_{72}$. The error bars were estimated by averaging the median difference values of the critical depth data point with the prior linear data point, and the first power law data point (Supplementary Figure S3 for details). (f) The estimated activation energies for the evolution of dealloying front at 2 × 10^{-4} Pa.

mation of possible errors. The error bars were obtained by averaging the median difference values of the critical depth point with the prior and the latter data points (Supplementary Fig. S3 for details). A higher dealloying temperature gives a larger critical value but shorter linear dealloying periods (Fig. 4e). The critical depth changes with the dealloying temperatures from ~23 μm at 653 K to ~30 μm at 723 K (Table 1), which is about 5 to 10 times larger than that of the corresponding pore sizes. Additionally, the critical values also show a weak composition dependence of the precursor alloys, which may be associated with the difference in the dealloyed microstructures. After the linear periods with the dealloying depths larger than the critical values, the time-depth relation can be well-described by the power law relation with the exponent value of 0.4 (the dotted fitting curves in Fig. 4b), which is the same as that of the VPD at 200 Pa (Fig. 3b).

3.3. Kinetic analysis of vapor phase dealloying

It has been suggested that the linear relation between dealloying depth and time (a constant dealloying rate) originates from interface-limited kinetics and a power law relation is due to a

Table 1
Experimental and calculated transition depths for the $Mn_{28}Zn_{72}$ and $Mn_{12}Zn_{88}$ systems.

Composition	Experimental critical depth x_t (μm)	Calculated critical depth (μm)	Corresponding average pore size d_t (nm)	x_t/d_t	$\frac{P_{ref}e^{\Delta S/R}e^{-\Delta H/RT}}{\sqrt{T}v_f}$	Tortuosity τ
$Mn_{28}Zn_{72}$-653 K	23.6±2.1	22.9	285±44	82.8	0.095	7.58
$Mn_{28}Zn_{72}$-673 K	29.5±3.6	37.6	429±61	68.8	0.156	14.99
$Mn_{28}Zn_{72}$-723 K	29.8±4.1	46.3	482±80	61.8	0.191	20.43
$Mn_{12}Zn_{88}$-653 K	23.2±4.2	15.0	396±44	58.6	0.051	5.75
$Mn_{12}Zn_{88}$-673 K	27.8±2.4	22.1	479±59	58.0	0.075	8.55
$Mn_{12}Zn_{88}$-723 K	31.6±2.5	28.0	673±147	46.9	0.095	13.39

The corresponding average pore size d_t at the critical depth, the ratio of x_t/d_t, $\frac{P_{ref}e^{\Delta S/R}e^{-\Delta H/RT}}{\sqrt{T}v_f}$ and the tortuosity are listed above.

diffusion-limited process in the dealloying medium [21,34]. The transition from linear to power law with dealloying depth under a lower pressure indicates that the dealloying kinetics may be controlled by an interface-limited process in the initial stage and changes to a long-range transport governed one with the development of pore channels after the sublimation of Zn. Linear interface-limited kinetics is described by an Arrhenius-type expression [28,39]:

$$v_f = Ae^{-\frac{E_a}{k_BT}} \tag{1}$$

where v_f is the dealloying front velocity, A is a concentration dependent prefactor, E_a is the activation energy for dealloying front propagation, k_B is the Boltzmann constant and T is the dealloying temperature. From the linear relationship between $\ln(v_f)$ and $1/T$ for both $Mn_{28}Zn_{72}$ and $Mn_{12}Zn_{88}$ (Fig. 4f), we can estimate the dealloying activation energies within the linear kinetic regime: E_{a1}=0.91 eV for $Mn_{28}Zn_{72}$ and E_{a2}=0.95 eV for $Mn_{12}Zn_{88}$. The measured activation energy for the sublimation of pure Zn under the dealloying conditions is ~0.88 eV (Supplementary Fig. S4 and Supplementary Text for details). Considering the slightly higher bonding energy of Zn-Mn than Zn-Zn, the dealloying activation energies are close to that of the Zn sublimation from Zn-Mn alloys and, thus, the interface-limited process is likely dominated by the Zn sublimation from the precursor alloys at the dealloying fronts.

Dealloying kinetics within the power law regime at time and depths greater than the critical values in Fig. 4e and Table 1 were analyzed by scaling the plots of dealloying depth *vs* time at different temperatures of each pressure using the re-scaled time $t' = t \times \exp(-E/k_BT)$ [21,22]. All the experimental data from different temperatures fall on one master curve for each alloy dealloyed under different pressures (Fig. 5). It is important to stress that this collapse is independent of the fit parameters linked to porosity and tortuosity involved in the commonly used analytical expression for Knudsen diffusion in pore channels. The activation barrier within the power law regime can be obtained by fitting the scaled power law relation and are estimated to be 1.20 eV for $Mn_{28}Zn_{72}$ and 1.34 eV for $Mn_{12}Zn_{88}$ at the 200 Pa, and are about the same, 1.19 eV for $Mn_{28}Zn_{72}$ and 1.25 eV for $Mn_{12}Zn_{88}$ at 2.0×10^{-4} Pa (Fig. 5).

4. Discussion

4.1. Kinetic model of diffusion-limited vapor phase dealloying

Our experimental observations and analyses suggest a hypothesis that the rate-limiting kinetics in VPD changes from an interface-controlled process to a long-range diffusion controlled one at the critical dealloying depth after the formation of porous microstructure. The long-range transport of sublimated Zn within pore channels may be the origin of the power-law relation in the time-dependent dealloying process. Under dealloying conditions of 653 K and 200 Pa, the mean free path of Zn as calculated by the kinetic theory of gases is larger than 195 μm, orders of magnitude larger than the pore size of nanoporous Mn (hundreds of nanometers). This means that diffusion through the pores as the dealloying front penetrates into the bulk can be approximately described by Knudsen diffusion where the diffusive flux $J(x,t)$ of Zn in the pore channels at depth x follows Fick's 1st Law:

$$J(x,t) = -D_K\frac{\partial n(x,t)}{\partial x} \tag{2}$$

where $n(x,t) = P^{Zn}(x,t)/RT$ is the average concentration of Zn atoms in the vapor at depth x that varies from zero at the outer edge of the dealloyed layer (used here as a fixed origin of the x-axis) to $x_f(t) > 0$ at the dealloying front, D_K is the Knudsen diffusivity, P^{Zn} is the vapor pressure of zinc and R is the gas constant; with this choice of origin of the x-axis, a diffusive flux of Zn atoms away from the dealloying front towards the outer dealloyed layer corresponds to $J(x,t) < 0$ in Eq. (2). Mass conservation at the dealloying front requires that the dealloying rate is balanced by the diffusive flux at the dealloying front, yielding

$$-J\big(x_f(t),t\big)\Omega = v_f C_a^{Zn} \tag{3}$$

where Ω is the atomic volume of Zn, C_a^{Zn} is the atomic fraction of Zn in the precursor alloy, and $v_f = dx_f/dt > 0$ is the velocity of the dealloying front.

The position of the dealloying front can be obtained by solving a one-dimensional (1D) free-boundary problem analogous to the one describing diffusion-limited LMD kinetics [21,22]. Here, this problem consists of solving the 1D diffusion equation $\frac{\partial n}{\partial t} = D_K\frac{\partial^2 n}{\partial x^2}$, which follows from Eq. (2) with the continuity relation $\frac{\partial n}{\partial t} + \frac{\partial J}{\partial x} = 0$, together with three boundary conditions corresponding to the mass conservation condition at the dealloying front (Stefan condition defined by Eq. 3) and the concentrations $n(x_f,t) = P_{eq}^{Zn}/RT \equiv n_f^{eq}$ and $n(0,t) = n_0$ at the dealloying front and the edge of the dealloyed layer, respectively, where $n_0 = P_0/RT$ is the background concentration of Zn in the chamber environment. When imposing the boundary condition $n(x_f,t) = n_f^{eq}$, we are assuming that the equilibrium vapor pressure has reached its equilibrium value at dealloying depths larger than a critical transition value x_t of the order of a few ligament widths. For $x_f > x_t$, sublimating Zn atoms are confined inside the nanoporous structure and undergo multiple reflections from surfaces, thereby allowing sufficient time for the vapor at the dealloying front to reach local thermodynamic equilibrium by the balance of detachment (sublimation) and reattachment of Zn atoms. In contrast, for $x_f < x_t$, a significant fraction of evaporating atoms can escape the dealloyed layer by ballistic motion with initially no reflection and thus negligible reattachments. In the initial stage of dealloying, the front velocity is expected to be controlled by the detachment rate and thus to be approximately constant with the activation energy of Zn sublimation following Eq. (1), consistent with our experimental observation of a linear relation in early dealloying regime $x_f \propto t$ for $x_f < x_t$ followed by a diffusion-limited regime $x_f \propto t^{1/2}$ for $x_f > x_t$.

To complete our analysis of the latter diffusion-limited regime and use the result later to estimate x_t, we assume that diffusion in-

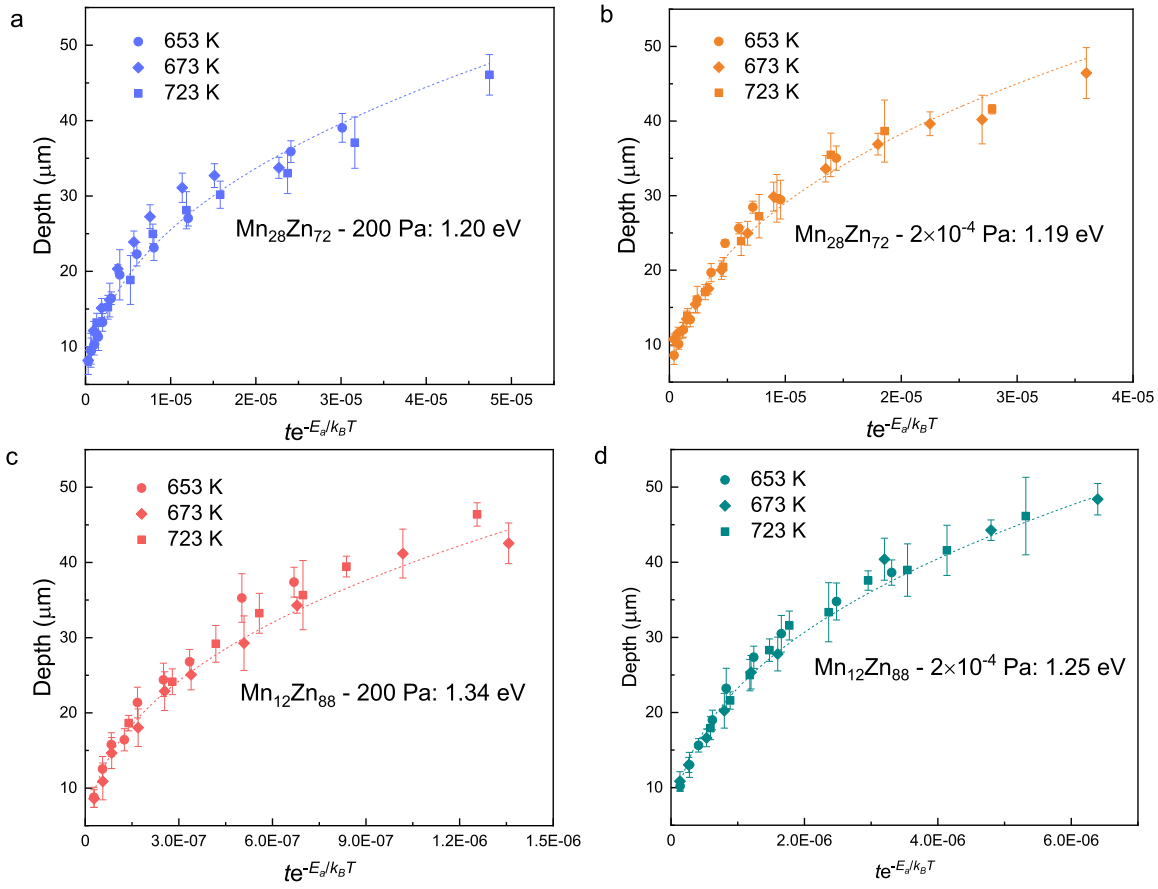

Fig. 5. Collapsed dealloying depth versus scaled time $t \times \exp(-E/k_BT)$ for (a) $Mn_{28}Zn_{72}$ at 200 Pa, (b) $Mn_{28}Zn_{72}$ at 2×10^{-4} Pa, (c) $Mn_{12}Zn_{88}$ at 200 Pa and (d) $Mn_{12}Zn_{88}$ at 2×10^{-4} Pa.

side the dealloyed layer is fast compared to the time scale of dealloying ($x_f v_f / D_K \ll 1$). Hence the concentration inside the dealloyed layer can relax quickly to the solution of the quasi-static diffusion equation $\frac{d^2 n(x)}{dx^2} \cong 0$, which gives the linear profile

$$n(x,t) \cong \frac{\left(n_f^{eq} - n_0\right)x}{x_f(t)} + n_0, \tag{4}$$

Combining Eqs. (2), (3) and (4) yields the differential equation for $x_f(t)$

$$\frac{dx_f(t)}{dt} \cong \frac{D_K \Omega}{C_a^{Zn}} \frac{\left(n_f^{eq} - n_0\right)}{x_f(t)}, \tag{5}$$

with solution

$$x_f^2 = \frac{2 D_K \Omega}{RT} \frac{\left(P_{eq}^{Zn} - P_0\right)}{C_a^{Zn}} t, \tag{6}$$

after converting from concentration to partial pressure using the ideal gas law. Next, we use the standard expression for the Knudsen diffusivity

$$D_K = \frac{\varepsilon}{\tau} \frac{d}{3} \left(\frac{8RT}{\pi M}\right)^{1/2}, \tag{7}$$

where d is the pore size and M is the mass of Zn in kg/mol. The factors ε and τ are the porosity and tortuosity factors, respectively [40]. Substituting Eq. (7) into Eq. (6) gives the final prediction for the dealloying depth during diffusion-controlled VPD in terms of basic morphological and control parameters:

$$x_f^2 = \frac{2}{3} \frac{\varepsilon}{C_a^{Zn}} \frac{d}{\tau} \left(\frac{8}{\pi M}\right)^{1/2} \frac{\Omega}{\sqrt{RT}} \left(P_{eq}^{Zn} - P_0\right) t. \tag{8}$$

In previous publications, the square root of time relation for the dezincification (mainly α- and β- brasses) is commonly explained by the Kirkendall effect by assuming that void formation is caused by the difference between the large outward flux of Zn atoms and the inward flux of Cu atoms [41,42]. However, the proposed mechanism of VPD involves the diffusive transport of Zn atoms in the vapor phase constrained inside the pore channels and driven by the concentration gradient from the dealloying front, where the vapor concentration of Zn atoms is determined by the equilibrium partial pressure, to the outer edge of the dealloyed layer where the concentration is determined by the environmental pressure. This new mechanism is supported by the collapse of the dealloying depth versus scaled time plots at different temperatures (Fig. 5), where the scaled time uses quantitatively the Arrhenius law for the equilibrium Zn vapor pressure.

4.2. Application to nanoporous Mn

The equilibrium vapor pressure appearing in Eq. (8) can be calculated from the Gibbs free energy difference between the solid and vapor phases via $P_{eq}^{Zn} = P_{ref} e^{\Delta S/R} e^{-\Delta H/RT}$, where P_{ref} is the standard pressure (10^5 Pa). Due to the steady gas flow (Ar: 200 sccm, H_2: 10 sccm) and continuous evacuation by the vacuum system during the dealloying process, dealloying occurs under forced-convection conditions and P_0 is negligible. Therefore, the dealloying depth *vs.* time is given by:

$$x_f^2 = \frac{2}{3} \frac{\varepsilon}{C_a^{Zn}} \frac{d}{\tau} \left(\frac{8}{\pi M}\right)^{1/2} \frac{\Omega}{\sqrt{RT}} P_{ref} e^{\Delta S/R} e^{-\Delta H/RT} t. \tag{9}$$

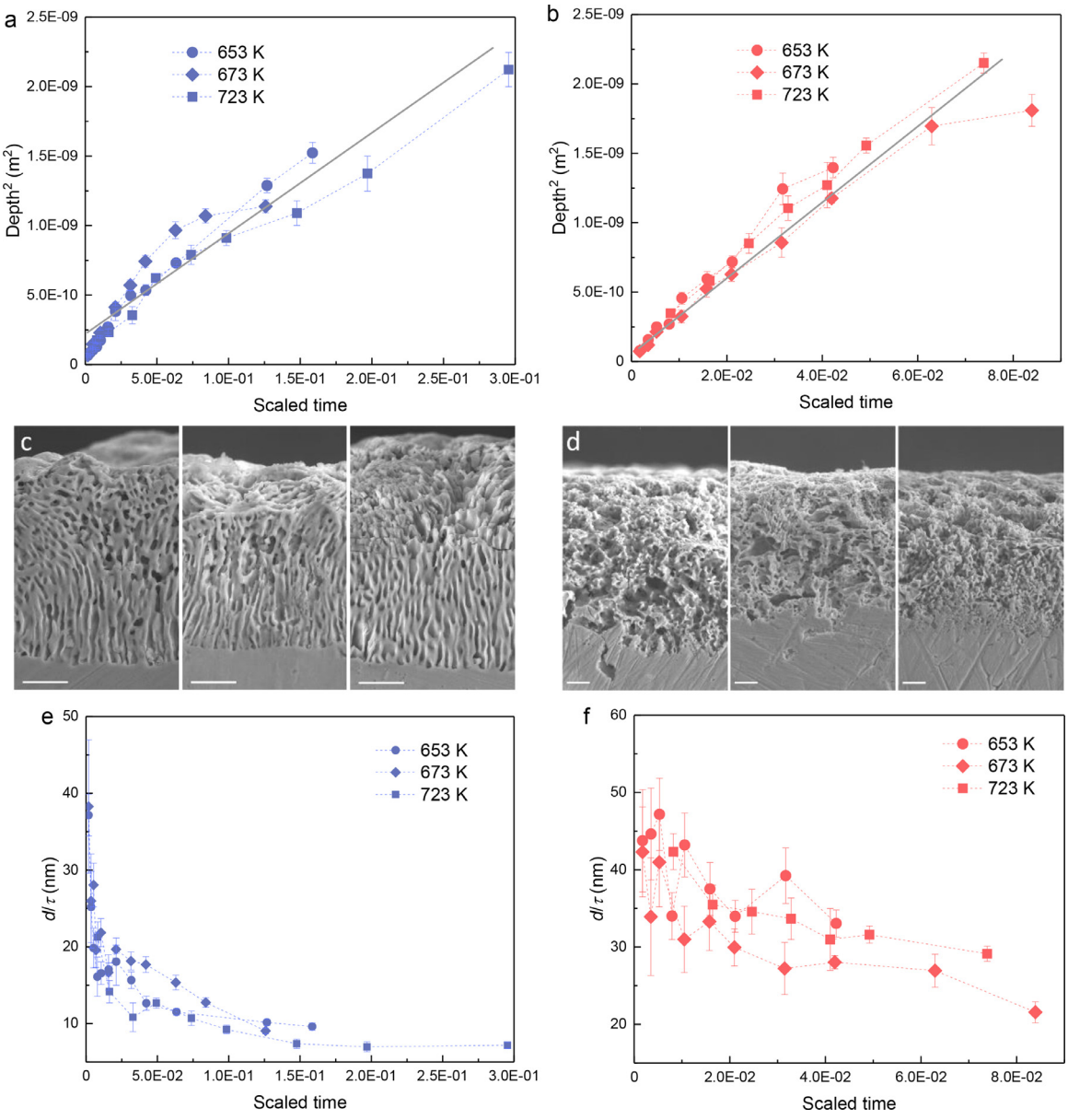

Fig. 6. Plots of x_f^2 vs. scaled time of $\frac{2}{3}\frac{\varepsilon}{C_a^{Zn}}\left(\frac{8}{\pi M}\right)^{1/2}\frac{\Omega}{\sqrt{RT}}P_{ref}e^{\Delta S/R}e^{-\Delta H/RT}t$ for (a) $Mn_{28}Zn_{72}$ and (b) $Mn_{12}Zn_{88}$ systems at 200 Pa. (c) Representative micrographs of $Mn_{28}Zn_{72}$ samples with nearly the same dealloying depth of 22 μm: (left) 653 K (t = 10,800 s), (middle) 673 K (t = 3,600 s), (right) 723 K (t = 1800 s). (d) Representative micrographs of $Mn_{12}Zn_{88}$ samples near a scaled time of 3.2 × 10^{-2}: (left) 653 K (t = 10,800 s), (middle) 673 K (t = 5,400 s), (right) 723 K (t = 1,200 s). Change in the d/τ ratio with scaled time for (e) $Mn_{28}Zn_{72}$ and (f) $Mn_{12}Zn_{88}$ systems at 200 Pa.

Less than 5% residual zinc was found in all samples after dealloying, so the porosity in any given sample will be approximately the alloy concentration, i.e., $\varepsilon \sim C_a^{Zn}$. The atomic volume of zinc is 9.16 cm^3/mol. The entropy and enthalpy of sublimation of pure Zn are well-known and available as a function of temperature from the NIST Chemistry WebBook [43]: $\Delta S^{Zn}/R$ =13.8 and ΔH^{Zn}=128 kJ/mol (1.33 eV/atom). Note that the value of 1.33 eV is close to the estimated barrier energies of power law relations for both $Mn_{12}Zn_{88}$ and $Mn_{28}Zn_{72}$ precursors. The only unknowns in Eq. (9) are d and τ, so we plot x_f^2 *vs.* the right-hand side of Eq. (9) divided by (d/τ), as shown in Fig. 6a and b. Good data collapse is seen for all three temperatures, with no fitting parameters for both $Mn_{12}Zn_{88}$ and $Mn_{28}Zn_{72}$. The approximately linear master curves suggest that the morphology and topology of dealloyed porous microstructure for each alloy are similar at different dealloying temperatures, as reflected in the similar (d/τ) values. Fig. 6c and d show representative micrographs of samples at a scaled time of 3.1 × 10^{-2} for $Mn_{28}Zn_{72}$ and 3.2 × 10^{-2} for $Mn_{12}Zn_{88}$ with similar morphologies, respectively. In contrast, the large difference in the slopes of the master curves of $Mn_{12}Zn_{88}$ and $Mn_{28}Zn_{72}$ in in Fig. 6a and b suggests that the morphology and topology of the dealloyed porous microstructure strongly depend on the chemical compositions of the precursors, which is well consistent with the SEM micrographs displayed in Fig. 6c and d. Fig. 6e and f show the evolution of d/τ with scaled time for $Mn_{28}Zn_{72}$ and $Mn_{12}Zn_{88}$, respectively. Over the course of porosity formation, d/τ reduces from a high value of ~40, leveling off near 10 for $Mn_{28}Zn_{72}$, and from 45 to 25 for $Mn_{12}Zn_{88}$. If the mean free path in the porous structure is a constant, this means there is an increase in tortuosity over the course of porosity formation with a factor of 4 and 1.8, respectively. If the final value of ranges over the typical τ~3-4 value, that would imply a mean free path in the pore size of order 100 nm, which is consistent with the length scale of porosity in the micro-

graphs. Moreover, the reduced d/τ, on account of the increasing of the tortuosity, could slow the growth of dealloying depth and modulate the diffusion-limited behavior with the development of dealloying (Eq. (9)). Consequently, the continuous changes of the tortuosity with dealloying may be the underlying reason that the experimental power law exponential (0.4) is lower than the theoretically yielded value of 0.5, which warrants future study in developing a comprehensive dealloying kinetic model with the consideration of the microstructural evolution during dealloying.

The Knudsen diffusion-based model for the interface velocity in VPD is consistent with both the thermodynamics and morphology of the materials under consideration here. It is interesting that the enthalpies of sublimation in the model assume *local equilibrium* between the vapor and solid at the dealloying front, and that Knudsen transport through the porous layer is essentially ballistic, with reflective walls. That there is possible deposition/resublimation along the channels of the dealloyed microstructure is likely reflective of the phase change in the porous Mn layer. The local interface equilibrium condition is more unusual in the context of evaporation into a vacuum. Indeed, when we measured the velocity of irreversible pure Zn evaporation (i.e., that does not form porosity) and extracts an activation energy of sublimation, we found a value of ΔH~0.9 eV (Supplementary Fig. S4). The apparent energy barrier for the power-law process of VPD is thus not an activation barrier at all, but the difference in the enthalpies of Zn in the solid and vapor phases, respectively; as such it should equal to the cohesive energy of Zn, which it does (1.35 eV). Microscopic reversibility thus suggests that the enthalpy difference between a Zn atom in the bulk and a Zn atom on the surface is approximately 0.4 eV, completing the energy landscape of evaporation in this system.

4.3. Cross-over between interface- and diffusion-limited dealloying kinetics

According to experimental observations and the kinetic model, the VPD of the Zn-Mn alloys involves two stages: (i) an interface-limited nonequilibrium dealloying process with the continuous increase of Zn partial vapor pressure at the dealloying front for dealloying depth $x_f < x_t$ with the front velocity described by Eq. (1); and (ii) a diffusion-limited dealloying process with the Zn vapor pressure at the dealloying front equal to its equilibrium value P_{eq}^{Zn} at the dealloying temperatures for $x_f > x_t$ with the front velocity described by Eq. (8) (or Eq. (9) using the expression for P_{eq}^{Zn}). While describing the complex transition regime where $x_f \sim x_t$ would require a considerably more elaborate model, a first rough estimate of the transition depth x_t can be obtained by computing the depth at which the front velocities for interface- and diffusion-limited dealloying processes have comparable magnitude. Setting $dx_f(t)/dt$ with $x_f(t)$ predicted by Eq. (9) equal to v_f predicted by Eq. (1) yields the estimate:

$$x_t = \frac{1}{3}\frac{d}{\tau}\left(\frac{8RT}{\pi M}\right)^{1/2}\frac{\varepsilon}{C_a^{Zn}}\frac{\Omega}{RTv_f}P_{ref}e^{\Delta S/R}e^{-\Delta H/RT}. \quad (10)$$

To test this prediction quantitatively, we used Eq. (10) to compute x_t using measured values of the front velocity v_f in the linear interface-limited regime listed in Supplementary Table together with the other parameters previously determined to characterize the diffusion-limited regime. The predicted values are listed in Table 1. For comparison, the critical transition depths and the corresponding pore sizes at different dealloying temperatures were carefully measured (Table 1). The experimental and predicted depths are reasonably consistent with each other and present a monotonic increase with dealloying temperature. When the environmental (dealloying) pressure is lower, this stage will be more obvious as a larger critical dealloying depth is required for a system to reach the dynamic equilibrium state at the dealloying front at which the Zn partial pressure is close to the saturated one at the corresponding dealloying temperatures. To further investigate the transition from linear to power law kinetics, we plotted the dealloying diagram on the basis of the Eq. (10), which presents the temperature T and environmental pressure P_0 dependence of the critical depth for $Mn_{28}Zn_{72}$ and $Mn_{12}Zn_{88}$ (Fig. 7). As a general tendency, the critical depth is more sensitive to temperature at a lower pressure. While, at a higher temperature it changes significantly with pressure. Based on the calculated critical depths x_t and measured pore sizes d_t, we can estimate the ratio of x_t/d_t. For both alloys, the ratios decrease with the increase of dealloying temperature. Meanwhile, since the ratio x_t/d_t can also be estimated by:

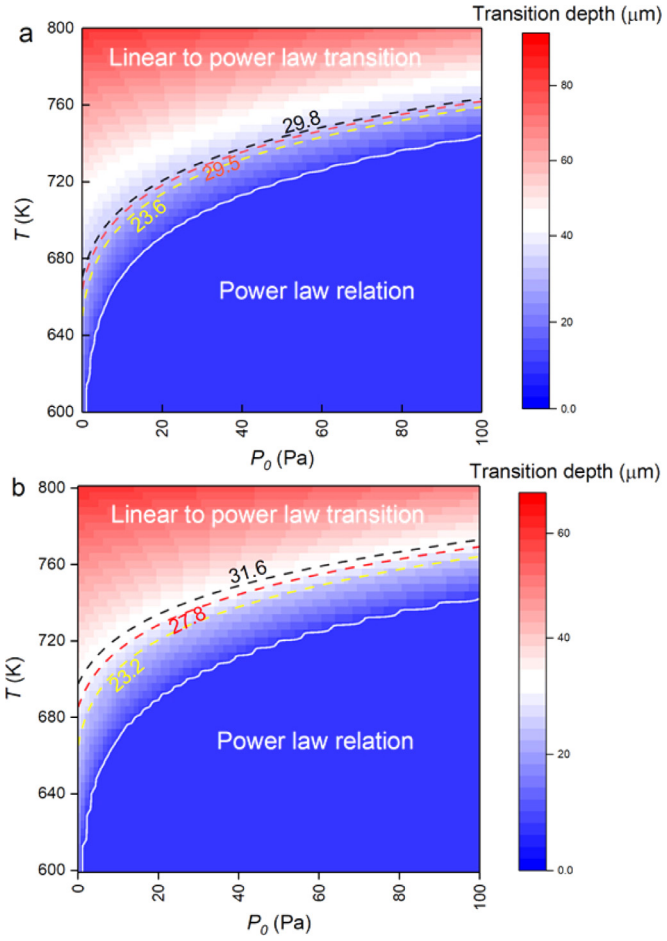

Fig. 7. The dealloying diagram showing the T and P_0 dependence of the critical transition depth x_t for (a) $Mn_{28}Zn_{72}$; and (b) $Mn_{12}Zn_{88}$.

$$x_t/d_t \propto \frac{1}{\tau}\frac{P_{ref}e^{\Delta S/R}e^{-\Delta H/RT}}{\sqrt{T}v_f}, \quad (11)$$

the value of $\frac{P_{ref}e^{\Delta S/R}e^{-\Delta H/RT}}{\sqrt{T}v_f}$ and thus the tortuosity τ of dealloyed porous microstructure at the critical depth can be calculated (Table 1). In contrast to the drops of x_t/d_t with the increase of dealloying temperature, the value of $\frac{P_{ref}e^{\Delta S/R}e^{-\Delta H/RT}}{\sqrt{T}v_f}$ increases. Therefore, the tortuosity increases with dealloying temperature and environment pressure, further verifying that the dealloyed microstructure evolves with the dealloying conditions and depends on the chemical compositions of precursor alloys.

5. Conclusions

In summary, we systematically investigated the kinetics of VPD using Zn-Mn alloys as the model system. The kinetics of VPD not only depends on the thermodynamic variables of pressure, temperature and precursor composition but also the depth and tortuosity of resulting pores. The interplay between dealloying kinetics and resulting microstructure results in the transition from interface-limited kinetics to diffusion-limited transport kinetics at a critical dealloying depth where Knudsen diffusion works. Our experimental observations and theoretical modeling suggest that the development of porous microstructure restricts vapor transport and leads to the linear increase of Zn vapor partial pressure from the environmental (dealloying) pressures to the saturated partial pressure of Zn at the dealloying front. Activation energy measurements verify that interface-limited kinetics is controlled by the evaporation of Zn at dealloying fronts while diffusion-limited kinetics are controlled by the mass transport of Zn in the pore channels with the effective activation barrier equal to the enthalpy difference of Zn in the solid and vapor phases.

Authors' contribution

M. C. conceived and supervised the research project. Z.L., D.X.W. and J.J. prepared the samples. Z.L. performed VPD experiments, SEM and XRD characterization. A. K. and J. E. developed theoretical models for diffusion-limited VPD kinetics and the equilibrium vapor pressure, respectively. Z. L., M. C. and M.Z. conducted data analysis. J.H.H., F.Z., Y.J.X, A.H. and K.W. contributed to VPD experiments. M. C, Z. L and J. E, wrote the paper. All authors contributed to discussion and manuscript writing.

Declaration of Competing Interest

We declare that we have no conflict of interest.

Acknowledgements

We thank Karl Sieradzki and Juergen Biener for inspiring discussion. This work was sponsored by JST-CREST "Phase Interface Science for Highly Efficient Energy Utilization", JST (Japan); and the Fusion Research Funds from WPI-AIMR, Tohoku University. M.C. acknowledges the support of U.S. National Science Foundation under grant DMR-1804320. J.E. thanks the U.S. National Science Foundation under grant DMR-1806142. A.K. acknowledges the support of Grant No. DE-FG02-07ER46400 from the U.S. Department of Energy, Office of Basic Energy Sciences.

Supplementary materials

Supplementary material associated with this article can be found, in the online version, at doi:10.1016/j.actamat.2021.116916.

Appendix A. Supporting information

Supplementary data associated with this article can be found in the online version.

References

[1] D.J. Tulimieri, J. Yoon, M.H.W. Chan, Ordering of helium mixtures in porous gold, Phys. Rev. Lett. 82 (1999) 121–124.
[2] T. Fujita, P. Guan, K. McKenna, X. Lang, A. Hirata, L. Zhang, T. Tokunaga, S. Arai, Y. Yamamoto, N. Tanaka, Y. Ishikawa, N. Asao, Y. Yamamoto, J. Erlebacher, M. Chen, Atomic origins of the high catalytic activity of nanoporous gold, Nat. Mater. 11 (2012) 775–780.
[3] B.C. Tappan, S.A. Steiner III, E.P. Luther, Nanoporous Metal Foams, Angew. Chem. Int. Ed. 49 (2010) 4544–4565.
[4] Q. Yang, S. Liang, B. Han, J. Wang, R. Mao, Preparation and properties of enhanced bulk nanoporous coppers, Mater. Lett. 73 (2012) 136–138.
[5] A. Wittstock, V. Zielasek, J. Biener, C.M. Friend, M. Bäumer, Nanoporous gold catalysts for selective gas-phase oxidative coupling of methanol at low temperature, Science 327 (2010) 319–322.
[6] V. Zielasek, B. Jürgens, C. Schulz, J. Biener, M.M. Biener, A.V. Hamza, M. Bäumer, Gold Catalysts, Nanoporous gold foams, Angew. Chem. Int. Ed. 45 (2006) 8241–8244.
[7] J. Zhang, C.M. Li, Nanoporous metals: fabrication strategies and advanced electrochemical applications in catalysis, sensing and energy systems, Chem. Soc. Rev. 41 (2012) 7016–7031.
[8] M.M. Biener, J. Biener, A. Wichmann, A. Wittstock, T.F. Baumann, M. Bäumer, A.V. Hamza, ALD functionalized nanoporous gold: thermal stability, mechanical properties, and catalytic activity, Nano Lett. 11 (2011) 3085–3090.
[9] J. Biener, A. Wittstock, L.A. Zepeda-Ruiz, M.M. Biener, V. Zielasek, D. Kramer, R.N. Viswanath, J. Weissmuller, M. Baumer, A.V. Hamza, Surface-chemistry–driven actuation in nanoporous gold, Nat. Mater. 8 (2009) 47–51.
[10] K. Hu, D. Lan, X. Li, S. Zhang, Electrochemical DNA biosensor based on nanoporous gold electrode and multifunctional encoded DNA–Au bio bar codes, Anal. Chem. 80 (2008) 9124–9130.
[11] S. Kondrat, C.R. Perez, V. Presser, Y. Gogotsi, A.A. Kornyshev, Effect of pore size and its dispersity on the energy storage in nanoporous supercapacitors, Energy Environ. Sci. 5 (2012) 6474–6479.
[12] J. Han, Y.C. Lin, L. Chen, Y.-C. Tsai, Y. Ito, X. Guo, A. Hirata, T. Fujita, M. Esashi, T. Gessner, M. Chen, On-chip micro-pseudocapacitors for ultrahigh energy and power delivery, Adv. Sci. 2 (2015) 1500067.
[13] X. Lang, A. Hirata, T. Fujita, M. Chen, Nanoporous metal/oxide hybrid electrodes for electrochemical supercapacitors, Nat. Nano 6 (2011) 232–236.
[14] Y.G. Guo, J.S. Hu, L.J. Wan, Nanostructured materials for electrochemical energy conversion and storage devices, Adv. Mater. 20 (2008) 2878–2887.
[15] J. Erlebacher, M.J. Aziz, A. Karma, N. Dimitrov, K. Sieradzki, Evolution of nanoporosity in dealloying, Nature 410 (2001) 450–453.
[16] Q. Zhang, Z. Zhang, On the electrochemical dealloying of Al-based alloys in a NaCl aqueous solution, Phys. Chem. Chem. Phys. 12 (2010) 1453–1472.
[17] K. Sieradzki, N. Dimitrov, D. Movrin, C. McCall, N. Vasiljevic, J. Erlebacher, The dealloying critical potential, J. Electrochem. Soc. 149 (2002) B370–B377.
[18] D.V. Pugh, A. Dursun, S.G. Corcoran, Formation of nanoporous platinum by selective dissolution of Cu from $Cu_{0.75}Pt_{0.25}$, J. Mater. Res. 18 (2003) 216–221.
[19] J.S. Yu, Y. Ding, C.X. Xu, A. Inoue, T. Sakurai, M.W. Chen, Nanoporous metals by dealloying multicomponent metallic glasses, Chem. Mater. 20 (2008) 4548–4550.
[20] M. Hakamada, M. Mabuchi, Preparation of nanoporous Ni and Ni–Cu by dealloying of rolled Ni–Mn and Ni–Cu–Mn alloys, J. Alloy Compd. 485 (2009) 583–587.
[21] I. McCue, B. Gaskey, P.-A. Geslin, A. Karma, J. Erlebacher, Kinetics and morphological evolution of liquid metal dealloying, Acta Mater. 115 (2016) 10–23.
[22] P.-A. Geslin, I. McCue, B. Gaskey, J. Erlebacher, A. Karma, Topology-generating interfacial pattern formation during liquid metal dealloying, Nat. Commun. 6 (2015) 8887.
[23] T. Wada, K. Yubuta, A. Inoue, H. Kato, Dealloying by metallic melt, Mater. Lett. 65 (2011) 1076–1078.
[24] T. Wada, T. Ichitsubo, K. Yubuta, H. Segawa, H. Yoshida, H. Kato, Bulk–nanoporous-silicon negative electrode with extremely high cyclability for lithium-ion batteries prepared using a top-down process, Nano Lett. 14 (2014) 4505–4510.
[25] J.D. Harrison, C. Wagner, The attack of solid alloys by liquid metals and salt melts, Acta Metall. Mater. 7 (1959) 722–735.
[26] Z. Lu, C. Li, J. Han, F. Zhang, P. Liu, H. Wang, Z. Wang, C. Cheng, L. Chen, A. Hirata, T. Fujita, J. Erlebacher, M. Chen, Three-dimensional bicontinuous nanoporous materials by vapor phase dealloying, Nat. Commun. 9 (2018) 276.
[27] J. Han, C. Li, Z. Lu, H. Wang, Z. Wang, K. Watanabe, M. Chen, Vapor phase dealloying: a versatile approach for fabricating 3D porous materials, Acta Mater. 163 (2019) 161–172.
[28] J. Erlebacher, An atomistic description of dealloying porosity evolution, the critical potential, and rate-limiting behavior, J. Electrochem. Soc. 151 (2004) C614–C626.
[29] J. Erlebacher, Mechanism of coarsening and bubble formation in high-genus nanoporous metals, Phys. Rev. Lett. 106 (2011) 225504.
[30] Q. Chen, K. Sieradzki, Mechanisms and morphology evolution in dealloying, J. Electrochem. Soc. 160 (2013) C226–C231.
[31] J. Weissmüller, K. Sieradzki, Dealloyed nanoporous materials with interface–controlled behavior, Mrs Bull. 43 (2018) 14–19.
[32] Q. Chen, K. Sieradzki, Spontaneous evolution of bicontinuous nanostructures in dealloyed Li-based systems, Nat. Mater. 12 (2013) 1102–1106.
[33] S. Parida, D. Kramer, C.A. Volkert, H. Rösner, J. Erlebacher, J. Weissmüller, Volume change during the formation of nanoporous gold by dealloying, Phys. Rev. Lett. 97 (2006) 035504.
[34] Y.-c.K. Chen-Wiegart, S. Wang, W.-K. Lee, I. McNulty, P.W. Voorhees, D.C. Dunand, In situ imaging of dealloying during nanoporous gold formation by transmission X-ray microscopy, Acta Mater. 61 (2013) 1118–1125.
[35] Y.-c.K. Chen-Wiegart, S. Wang, I. McNulty, D.C. Dunand, Effect of Ag–Au composition and acid concentration on dealloying front velocity and cracking during nanoporous gold formation, Acta Mater. 61 (2013) 5561–5570.
[36] M. Tsuda, T. Wada, H. Kato, Kinetics of formation and coarsening of nanoporous α-titanium dealloyed with Mg melt, J. Appl. Phys. 114 (2013) 113503.

[37] I. McCue, A. Karma, J. Erlebacher, Pattern formation during electrochemical and liquid metal dealloying, Mrs Bull. 43 (2018) 27–34.
[38] D.R. Lide, CRC Handbook of Chemistry and Physics, 84th ed, CRC Press, Boca Raton (FL), 2003.
[39] M.C. Tai, A. Gentle, M.D. Arnold, M.B. Cortie, Optical in situ study of de-alloying kinetics in nanoporous gold sponges, Rsc. Adv. 6 (2016) 85773–85778.
[40] J. Kärger, D.M. Ruthven, D.N. Theodorou, Diffusion in Nanoporous Materials, Wiley-VCH, Weinheim, 2012.
[41] I. Itoh, T. Hikage, Dezincification mechanism of brass in vacuum at high temperature, Trans. Jpn. Inst. Met. 17 (1976) 165–169.
[42] A. Craievich, A. Guinier, Cavités submicroscopiques dans le laiton dézincifié, Acta Metall. 21 (1973) 1327–1333.
[43] P.J. Linstrom, W.G. Mallard, NIST Chemistry WebBook; NIST Standard Reference Database Number 69., National Institute of Standards and Technology, 2011 http://webbook.nist.gov.